Title
Exploration of the bio-analogous asymmetric C—C coupling mechanism in tandem CO2 electroreduction

Journal
Nature Catalysis, 5(10)

ISSN
2520-1158

Authors
Chen, Chubai
Yu, Sunmoon
Yang, Yao
et al.

Publication Date
2022-10-01

DOI
10.1038/s41929-022-00844-w

Exploration of the bio-analogous asymmetric C-C coupling mechanism in tandem CO_2 electroreduction

Chubai Chen[1,3,6], Sunmoon Yu[2,3,6], Yao Yang[1,4], Sheena Louisia[1,3], Inwhan Roh[1], Jianbo Jin[1], Shouping Chen[2,3], Peng-Cheng Chen[1,5], Yu Shan[2,3], Peidong Yang[1, 2, 3, 5, *]

[1]Department of Chemistry, University of California, Berkeley, CA, USA.

[2]Department of Materials Science and Engineering, University of California, Berkeley, CA, USA.

[3]Chemical Sciences Division, Lawrence Berkeley National Laboratory, Berkeley, CA, USA.

[4]Miller Institute for Basic Research in Science, University of California, Berkeley, CA, USA.

[5]Kavli Energy NanoScience Institute, Berkeley, CA, USA.

[6]These authors contribute equally.

Abstract: C-C coupling is a critical step of CO_2 fixation in constructing the carbon skeleton of value-added multicarbon products. Wood-Ljungdahl pathway is an efficient natural process through which microbes transform CO_2 into methyl and carbonyl and subsequently couple them together. This asymmetric coupling mechanism remains largely unexplored in inorganic CO_2 electroreduction. Herein, we experimentally validate the asymmetric coupling pathway through isotope-labeled co-reduction experiments on Cu surface where $^{13}CH_3I$ and ^{12}CO are co-fed externally as the methyl and the carbonyl source, respectively. Isotope-labeled multicarbon oxygenates were detected, confirming the electrocatalytic asymmetric coupling on the Cu surface. We further employed tandem Cu-Ag nanoparticle systems where $*CH_x$ and *CO intermediates can be generated to achieve asymmetric C-C coupling for practical CO_2 electroreduction. We found that the production of multicarbon oxygenates is correlated with the generation rate of two intermediate indicators: CH_4 and CO. By aligning their rates, the oxygenates generation rate can be maximized.

Main text

Electrochemical CO_2 reduction reaction (CO_2RR) has been regarded as a promising technology to help achieve carbon neutrality before 2070[1]. Therefore, a wide range of research has been stimulated aiming to convert CO_2 into value-added multicarbon chemicals with more control over catalytic selectivity[2-5]. However, as a principal step in constructing carbon skeletons, the C-C coupling mechanism in CO_2 fixation chemistry still needs further investigation as it is not yet well understood.

Interestingly, some bacteria in nature can digest CO_2 through the Wood–Ljungdahl metabolic pathway (W-L pathway) and efficiently transform it into acetate with complete selectivity. In the past decades, extensive research efforts have been made to reveal the underlying mechanisms of CO_2 transformation and C-C coupling in the W-L pathway, and a molecular-level understanding has been established[6-7]. CO_2 molecules are first converted into methyl groups and carbonyl groups in western and eastern branches of this pathway, respectively. These two groups then go through asymmetric C-C coupling with the assistance of acetyl-CoA synthase, resulting in acetate production (Fig. 1a).

For direct CO_2 electroreduction, copper (Cu) has attracted significant attention as a catalyst among many other inorganic materials since it is the only metal that can activate C-C coupling and therefore generate products beyond C_1 chemistry (C_2H_4, C_2H_5OH, CH_3COOH, n-C_3H_7OH, etc.). However, due to the complexity of CO_2 reduction on the Cu surface, understanding the coupling process on the Cu surface is still regarded as one of the central challenges in CO_2RR after decades of research[2, 8]. Currently, it is widely accepted that carbon monoxide (CO) generated from CO_2RR is the key intermediate for symmetric C-C coupling[9-10]. One compelling experimental evidence is that the potential window and product spectrum of both CO reduction and CO_2 reduction shows a high degree of consistency[11]. Nevertheless, there is still a lack of a comprehensive and convincing molecular picture of such C-C coupling. While some density functional theory (DFT) calculations and *in situ* spectroscopic evidence support the direct CO-CO dimerization on the Cu surface (*CO-*CO)[12-14], some other reports indicate that the protonation of *CO towards either hydroxymethylidyne (*COH) or formyl (*CHO) prior to C-C coupling is more thermodynamically favored under acidic to neutral pH[15-17]. Accordingly, *COH or *CHO could participate in the downstream C-C coupling. However, the exact role of these two intermediates is also debatable[16, 18-20]. The lack of consensus can be attributed to several factors: significant dependence of DFT results on modeling and algorithms, and non-negligible impact of experimental conditions associated with the catalytic sensitivity, including but not limited to applied potentials, surface pH, Cu active sites, electrolyte species, and surface modifiers within the double layer[21-25].

Although the asymmetric coupling between *CO and *CHO (*COH) has been explored for CO_2RR, very few of the efforts go further to discuss the possibility of the Wood–Ljungdahl pathway-like *CH_3 and *CO coupling in inorganic aqueous CO_2 electrolysis. One important reason why the study of asymmetric coupling is hampered is due to the challenge in correlating the experimentally detected *CH_x (x=1-3) signals in the *operando* spectrum to any particular intermediates or process[26-27]. Recently, some studies proposed that the *CH_x-*CO asymmetric coupling may happen under a CO concentrated environment (either generated by tandem catalyst architecture[28-29] or high-pressure CORR[30]) and contribute to the final product selectivity. The feasibility of asymmetric *CH_x-*CO coupling was theoretically studied and found to be energetically and kinetically possible on some specific Cu sites[28-29]. Nevertheless, without firm experimental evidence, it is still uncertain whether Cu has the ability to achieve asymmetric coupling on its surface during aqueous CO_2 electrolysis. The product spectrum of asymmetric coupling and the corresponding conversion mechanism is also unclear at this point.

Here, we designed co-reduction experiments to verify the catalytic capability of Cu surfaces for asymmetric *CH_3-*CO coupling by using an electropolished Cu foil. In order to circumvent the dilemma that it is difficult to specify intermediates from the spectrum, we assured the existence of the intermediates by externally feeding the CO and CH_3I as the two distinct intermediate sources. While *CO comes from the adsorption of CO gas, *CH_3 is electrochemically generated from CH_3I. By further labeling CH_3I with ^{13}C isotope, the verification of ^{13}C-^{12}C asymmetric coupling became technically feasible via nuclear magnetic resonance (NMR) spectroscopy. During the electrolysis of CH_3I, we found that a portion of the generated methyl group can be stabilized on the Cu surface even in a highly polar aqueous electrolyte. These methyl groups can then participate in the C-C coupling reaction and be coupled with another *CH_3 or *CO, generating several multicarbon products (C_2H_6, CH_3CHO, C_2H_5OH, CH_3COOH, $(CH_3)_2CO$) on the Cu surface. After the asymmetric coupling ability of Cu was confirmed, we moved to more practical CO_2 reduction electrocatalysis with a tandem Cu-Ag nanoparticle assembly. Analogous to the Wood–Ljungdahl pathway, Cu is responsible for *CH_x intermediates generation and Ag is for most of the *CO in this tandem system. Since directly quantifying the concentration of the intermediates on the Cu surface is a grand challenge under dynamic electrochemical conditions[31], we utilized the production rates of CH_4 and CO as a proxy for the availability of *CH_x and *CO intermediate in the catalytic microenvironment. The rate of CH_4 and CO can be tuned by changing the Cu-Ag ratio and the applied potential. A maximum multicarbon oxygenates generation rate was achieved when the CH_4 and CO production rates were aligned.

Results

Dehalogenation of CH_3I on electrified Cu surface.

In order to investigate asymmetric *CH_3-*CO coupling on the Cu surface (Fig. 1b,c), electrochemically polished Cu foil (EC-Cu) was chosen as a model Cu catalyst for the co-reduction experiments. The representative surface morphology of Cu foil before and after electrochemical polish (Supplementary Fig. 1a,b) was characterized by a scanning electron microscope (SEM). It was found that most of the rough features on the pristine Cu foil disappeared after the polish, giving a smoother surface. Meanwhile, double-layer capacitance measurement showed that the specific capacitance of EC-Cu decreased from 187.8 μF/cm^2 to 54.3 μF/cm^2 (Supplementary Figure 1c), which is a typical value for the EC-Cu and is consistent with the previous reports[32]. Elemental information of EC-Cu was also collected through X-ray photoelectron spectroscopy (XPS) to track the potential contamination after electrolysis (Supplementary Fig. 2). The only increased signals can be attributed to the surface absorbed iodine stemming from the electrolysis of CH_3I.

Alkyl halides are widely used as alkylating reagents in organic[33] and electro-organic[34] synthesis. Specifically, CH_3I was selected as the methyl providing reagent in this study, considering the solubility of CH_3I in aqueous electrolyte, the convenience of reaction product analysis, and the fact that the electrochemical dehalogenation process of CH_3I on metal foils were also preliminarily reported[35]. By monitoring the composition of gas effluent, we confirmed that no gas-phase product was generated through thermochemical processes such as radical reactions when CH_3I and EC-Cu co-exist in an aqueous electrolyte under open-circuit potential (Supplementary Fig. 3). The polarization response curve of CH_3I reduction reaction (CH_3IRR) on EC-Cu has been first explored to examine the potential window of *in situ* methyl generation in our system (Fig. 2a). Unlike the background curve representative of hydrogen evolution reaction (HER) under Ar atmosphere, the addition of CH_3I generates a distinctively strong electroreduction peak. The onset potential is around -0.1V vs reversible hydrogen electrode (RHE). It is worth noting that Cu does not behave as an inert electrode, but exhibits its catalytic behavior towards CH_3IRR. The onset potential of the same reaction on a glassy carbon electrode is more than 200 mV negative along with a much smaller cathodic peak, relative to that on Cu. The higher dissociation kinetics of CH_3I on the Cu surface may be attributed to the affinity between Cu and I[36].

To further explore the influence from electrolysis induced surface pH variation, pH-dependent CH_3IRR was also conducted (Fig. 2b). No noticeable peak shift was observed under the scale of standard hydrogen electrode (SHE) when electrolyte was changed from 0.1 M $KHCO_3$ to 0.1 M K_2CO_3 and 0.1 M KOH, indicating that any proton concentration effect on CH_3I dissociation if existing is negligible. Chronoamperometry experiments were then used to further study the potential dependency of CH_3IRR. The reduction products were collected and identified by gas chromatography (GC) and NMR spectroscopy. We found that CH_4 and C_2H_6 are the only two products generated from CH_3IRR (Fig. 2c) while H_2 and CH_3OH are two by-products derived from HER and CH_3I hydrolysis, respectively. It was also found that the production ratio between C_2H_6 and CH_4 is potential dependent. Under -0.2 V vs RHE, a 67.7% Faraday efficiency (FE) towards CH_4 and a 27.5% FE towards C_2H_6 were achieved. The C_2H_6 FE decreased down to 0% when -1 V

vs RHE was applied, where HER became a dominant reaction. This observation suggests that the methyl generation and C-C coupling are likely to be mediated by the Cu surface – although the C-C coupling step may be a non-electrochemical process – while competing with the H_2 evolution. It is worth noting that CH_3I is not the only reagent that can be electrochemically reduced to methyl group on Cu surface. Generally, we believe that $*CH_x$ can be generated by electrochemical dehalogenation reactions of various halomethanes and polyhalomethanes under similar conditions[37].

Asymmetric coupling in $^{13}CH_3I$ and ^{12}CO co-reduction.

CO was then introduced into the electrolysis system as another important building block in C-C asymmetric coupling on Cu surface. As a reference, the CO self-coupling ability on EC-Cu within the potential window from -0.2 to -1.0 V vs RHE was also shown in Fig. 3a. Due to the low solubility and inert property of CO in 0.1 M $KHCO_3$ electrolyte[11], multicarbons generated from CO reduction reaction (CORR) can only be detected under the potentials negative than -0.8V vs RHE and the total FE towards CORR is less than 10%. Despite being minor products, the liquid product signals from CO self-coupling (Fig. 3b) still can introduce uncertainty if they are not appropriately differentiated from the signals from CH_3-CO asymmetric coupling products.

The introduction of a ^{13}C isotope labeled reactant into the experiment is an effective method to remove this uncertainty. Specifically, the presence of a ^{13}C atom will induce the characteristic coupling to the surrounding protons and makes them distinguishable in the ^1H NMR spectrum. The co-reduction experiments were executed with CO gas and liquid-phase $^{13}CH_3I$ as the starting chemicals. No new gas product was observed from GC. With similar product species and potential dependency, the gas product spectrum appears to result from the combination of $^{13}CH_3IRR$ and $^{12}CORR$ (Fig. 3c). Nevertheless, several sets of the new proton peaks previously absent in the CORR-only spectrum were identified in the NMR spectrum, which were rigorously assigned to the four multicarbon oxygenates generated through $^{13}CH_3$-^{12}CO asymmetric coupling (Fig. 3e). Importantly, these asymmetric coupling products do not show up under the open circuit potential (OCP) while all other conditions are kept the same. These results indicate that this co-reduction reaction is an electrocatalytic process and the corresponding equations are proposed as follow (eq. 1-4):

$$*CH_3+*CO+H_2O+e^- \xrightarrow{\text{electrolysis on Cu}} CH_3CHO+OH^- \quad (1)$$

$$*CH_3+*CO+3H_2O+3e^- \xrightarrow{\text{electrolysis on Cu}} CH_3CH_2OH+3OH^- \quad (2)$$

$$2*CH_3+*CO \xrightarrow{\text{electrolysis on Cu}} (CH_3)_2CO \quad \text{or} \quad *CH_3+*CO+CH_3I+e^- \xrightarrow{\text{electrolysis on Cu}} (CH_3)_2CO+I^- \quad (3)$$

$$*CH_3+*CO+H_2O \xrightarrow{\text{electrolysis on Cu}} CH_3COOH+*H \quad (4)$$

The potential-dependent generation amounts of isotope labeled multicarbon oxygenate were also quantified to further understand the asymmetric coupling process (Fig. 3d). We found that the multicarbon oxygenate production amounts resulting from asymmetric coupling after 6 hours electrolysis first increases from 310 nmol/cm^2 Cu to 1972 nmol/cm^2 Cu when the applied potential switches from -0.2 V to -0.8 V vs RHE, as the CH_3IRR partial current density increases, and the absorption of CO on Cu becomes also stronger[38-39]. Further increasing the applied potential to -1.0 V vs RHE inhibits the asymmetric coupling. This can be attributed to the overwhelming HER and competitive CORR pathways. Acetaldehyde (CH_3CHO) is a major product in the co-reduction experiments under the wide potential range, generated by either the hydrogenation of $*CH_3$-*CO asymmetric coupling intermediate or the coupling between $*CH_3$ and *CHO. Based on the observation from CH_3IRR and CORR (Figs. 2c and 3a), and the spectroscopical evidence in literatures[14, 18], the hydrogenation of CO requires a large overpotential. Therefore, the coupling between $*CH_3$ and *CO is more likely to be the first step. Ethanol (CH_3CH_2OH) was found to be another asymmetric coupling product existing from -0.6 V to -1.0 V vs RHE, which can come from the further electroreduction of CH_3CHO[40]. It is worth noting that although H_2O is illustrated as one of the proton sources in eq. 1 and eq. 2, the proton can be actually more broadly derived from bicarbonate and *H in HER.

Acetic acid (CH_3COOH) and acetone ($(CH_3)_2CO$) were also found as two minor products from the isotope labeled co-reduction experiments. Instead of being hydrogenated, acetic acid and acetone are produced through further coupling processes between the $*CH_3$-*CO intermediate with H_2O or $*CH_3/CH_3I$. Although the generation amounts of CH_3COOH and $(CH_3)_2CO$ are influenced by the applied potential, they are not as potential-sensitive as CH_3CHO and CH_3CH_2OH. Nevertheless, it is worth noting that CO (or CO_2) insertion-type reaction mechanism with $*CH_x$ was previously proposed for acetic acid and acetone formation in thermal catalysis[41-43]. To verify whether CO_2 can also directly participate in the asymmetric coupling process with $*CH_3$ as an alternative pathway to generate acetate, potential dependent $^{12}CO_2$ and $^{13}CH_3I$ co-reduction experiments were also conducted (Supplementary Fig. 4). Interestingly, no C-13 labeled acetate can be observed in these experiments, indicating the coupling between $*CH_3$ and CO_2 or $*CO_2^{\cdot-}$ was prohibited. We propose that free CO_2 molecules have a linear configuration, which have a large steric hindrance and need to go through Eley-Rideal insertion mechanism, which requires a large activation energy. Meanwhile, the activated $*CO_2^{\cdot-}$ on electrified catalyst surface can be transformed into downstream intermediates quickly[44]. More mechanistic work is desired in the future to solidify these reaction mechanisms.

On the other hand, free I^- was generated during the CH_3I reduction process, which may interfere with Cu surface property and play a role in the co-reduction reaction[18]. To verify the potential influence of the I^- in the system, a control CORR experiment was conducted

where KI was added to the electrolyte (0.1 M $KHCO_3$) to match up the theoretical I^- concentration as in co-reduction reactions. As exhibited in Supplementary Fig. 5, no significant improvement in multicarbon generation amount was found in this KI-added CORR experiment. Although the current result cannot completely preclude all the possible positive effects of the trace amount of surface adsorbed iodine, it confirmed that this trace amount of the I^- in the system does not influence the isotope labeled co-reduction experiment results.

Optimizing tandem CO_2 electrolysis via asymmetric coupling.

The co-reduction experiments using two individual intermediates sources combined with isotope labeling provided us with strong evidence on $*CH_3$-*CO asymmetric coupling on a model EC-Cu system. We then further extended the research objectives from model system-based mechanism exploration to practical CO_2 electrolysis with nanocatalysts to advance our understanding of asymmetric coupling. To this end, a Cu-Ag bimetallic nanoparticle (NP) assembly was employed as the catalytic platform to explore the asymmetric coupling in CO_2RR. The colloidal synthesis of both 7nm Cu and 7nm Ag NPs followed our group's previously developed methods[44-46]. As an electrochemical tandem design principle, Ag can serve as a CO generator while Cu as a $*CH_x$ generator[28-29] (equivalent to carbonyl and methyl branch in the W-L pathway, respectively) for such asymmetric coupling. According to previous research, the Cu NPs on glassy carbon exhibit high selectivity towards methane[47] while Ag NPs were found to be a good CO-producing catalyst with nearly unity FE[44]. While the intermediates on the Cu are hard to be directly probed during electrolysis, CO and CH_4 generation rates can be easily measured and serve as an alternative way to indirectly monitor the corresponding surface chemistry. Therefore, we chose a potential range where Ag NPs selectively produce CO while Cu NPs generate CH_4 as the main product.

The prepared monodisperse 7nm Cu NPs (Fig. 4a) and Ag NPs (Fig. 4b) were spin-coated onto a glassy carbon electrode to form a dense monolayer, which was then used for CO_2RR (Fig. 4c). Post-electrolysis characterization of Cu-Ag NPs was also conducted to explore any other possible factors besides the tandem effect that may influence the catalytic performance. Scanning electron microscopy (SEM) imaging, scanning transmission electron microscopy (STEM) imaging, together with energy dispersive and electron energy loss spectroscopy (EDX and EELS) elemental mapping, show that Cu NPs migrated and agglomerated, forming a network during the CO_2 electrolysis due to the dynamic nature of Cu NPs (Supplementary Figs. 6 and 7). Ag particles were found to grow larger but remain isolated on the Cu-Ag network. The nanodomains and the interfaces between Ag and Cu were further characterized by HR-TEM (Supplementary Fig. 8). These results suggest that the Cu and Ag domains are in close contact with each other during CO_2RR rather than spatially separated on the as-prepared glassy carbon electrode. The XPS spectra of Cu and Ag indicate that no appreciable electronic interaction between Cu and Ag exists (Supplementary Fig. 9)[48].

Although $*CH_3$ generation in the co-reduction experiments can happen at potentials as positive as -0.1 V vs RHE due to external feeding of CH_3I reagent, the hydrodeoxygenation of *CO intermediates to $*CH_x$ intermediates on Cu during CO_2RR usually happens under relatively negative potentials. Pure Cu NP assembly, which is denoted as Cu100, was found to produce a significant amount of CH_4 within the potential window from -1.05 to -1.35 V vs RHE (Fig. 4d). A maximum CH_4 production rate of 4.66 nmol/s was achieved at -1.2 V vs RHE. When a more negative potential was applied, the overwhelming HER suppresses the CO_2 chemistry on Cu. Taking advantage of the tandem strategy, a certain fraction of the Cu NPs was replaced with Ag NPs to tune the catalytic CO_2 transformation rates towards both CO and CH_4. By increasing the Ag NP ratio from 0% to 50%, CO generation rate at -1.2 V vs RHE was enhanced from 0.22 nmol/s to 2.95 nmol/s. Meanwhile, since CO is a key intermediate in the production of CH_4 and functions as a competing adsorbate that suppresses HER, the generation of CH_4 on Cu sites may also benefit from the addition of Ag, especially under relatively negative potentials.

An aligned production rate of CO and CH_4 was achieved with Cu50Ag50 at -1.2 V vs RHE. Under such conditions, a 0.73 nmol/s production rate towards multicarbon oxygenates was observed on Cu50Ag50, which is 9.6 times higher than that on Cu100. To corroborate the early observation in the isotope co-reduction experiments, the correlation between multicarbon oxygenate production rates in tandem CO_2RR and the production rate of CO and CH_4 were also analyzed (Fig. 4e). While the asymmetric coupling needs both *CO and $*CH_x$ intermediates on the Cu surface, we defined the lower value between CO and CH_4 production rate under a particular reaction condition as a rate-determining dimensionless indicator to describe the co-existence of CH_4 and CO. Taking CO_2RR on Cu50Ag50 as an example, the production rate of CO and CH_4 under -1.2 V vs RHE are 2.75 and 2.95 nmol/s respectively. Therefore, the value representing the co-existence of CH_4 and CO is then defined as 2.75. It was found that the production rates of oxygenates obey well the same trend as the co-existence of CH_4 and CO value change. Even though the apparent production rates alone are not sufficient to further discuss the causality, a strong correlation between the two can be confirmed. Since a similar phenomenon and trend can be observed in both the electrochemical tandem CO_2RR and the isotope co-reduction experiments, our study suggests possible asymmetric coupling pathways for multicarbon products, which leads to a catalytic selectivity shift towards oxygenates.

Discussion

From this study, we envision that various tandem systems can be devised for more efficient and selective electrocatalytic CO_2-to-multicarbon oxygenate conversion, benefiting from the W-L pathway inspired asymmetric coupling. Thus far there have been significant advances in the development of efficient CO-producing (i.e., carbonyl branch) catalysts[49]. However, conventional Cu-based

catalysts typically require large overpotentials for $*CH_x$ generation. Therefore, it would be of great importance to developing improved catalysts (i.e., methyl branch) containing reaction sites, which not only can achieve efficient production of $*CH_x$ intermediates with high surface coverage at low overpotentials but also can facilitate the asymmetric coupling for selective multicarbon oxygenate product generation. In addition, systematic optimizations will be needed for the spatial distribution of the two distinct catalysts in the tandem system and the production rates of the two intermediates to attain improved catalytic results. Furthermore, microkinetic modeling studies are desired to scrutinize the impact of a microenvironment created by such tandem systems on the catalytic selectivity.

Conclusion

In summary, inspired by the Wood-Ljungdahl metabolic pathway, we explored asymmetric C-C coupling in CO_2RR by both the isotope labeled co-reduction experiments and Cu-Ag electrochemical tandem catalysis in more practical CO_2 electroreduction conditions. We initially validated the characteristic catalysis process of $*CH_3$-*CO asymmetric coupling on a Cu surface. Since the C-C coupling intermediate species are challenging to be directly probed, we developed an isotope labeled co-reduction process to explore the $*CH_3$-*CO coupling on Cu. Within a wide potential window, asymmetric $*CH_3$-*CO coupling can happen on Cu and yield up to four detectable isotope labeled oxygenate products including acetaldehyde, ethanol, acetic acid, and acetone. Hydrogenation is necessary for the production of acetaldehyde and ethanol from the asymmetric coupling intermediate, while acetic acid and acetone are generated through an additional coupling process. After confirming the Cu catalyzed asymmetric C-C coupling in the model system, a Cu-Ag nanoparticle assembly was used as a tandem catalyst for CO_2 electroreduction in order to further explore the asymmetric coupling in more practical conditions. The production rate of $*CH_x$ and *CO intermediates during CO_2RR can be successfully tuned by varying the nanoparticle number (and thus mass) ratio between Cu and Ag in the tandem system. The final generation rates of oxygenates are found to be strongly correlated with the co-existence of both intermediates. Maximized oxygenate generation rate can be achieved when those of the two intermediates are broadly aligned. These new insights of the C-C coupling pathway in CO_2 fixation not only confirmed the existence of asymmetric coupling, as another pathway in addition to the well explored *CO-*CO symmetric coupling pathway but also shed light on the new design paradigm of tandem catalytic systems in future CO_2 electrolysis.

Methods

Materials

Commercial Cu foil (thickness 0.25 mm, 99.98% trace metals basis), deuterium oxide (D_2O, 99.9 atom % D), methyl iodide (contains Cu wire as the stabilizer, 99.5%), o-phosphoric acid (85%, Supelco®), carbon rod (L150mm, Diam. 6mm, 99.995% trace metals basis), potassium bicarbonate ($KHCO_3$, ACS reagent, 99.7%), potassium carbonate (K_2CO_3, 99.995% trace metals basis), potassium hydroxide (KOH, 99.99% trace metals basis), dimethyl sulfoxide (DMSO, ACS reagent, ≥99.9%), potassium iodine (KI, ACS reagent, ⩾99.0%) and airbag (Supel™-Inert Multi-Layer Foil) were purchased from Sigma-Aldrich. Commercial Ag foil (thickness 0.28 mm, 99.9% trace metals basis) and Platinum gauze (99.9% metal basis) were ordered from Alfa Aesar. Glassy carbon electrode (CHI104) and Ag/AgCl (3M KCl) reference electrodes were purchased from CH Instrument and World Precision Instruments. Glassy carbon plate (25 mm×25 mm) was purchased from SPI supplies, and glassy carbon planchet (Dia. 25 mm) was purchased from Ted Pella. Carbon monoxide (4.0 research), Carbon dioxide (CO_2, 4.5LS), and Argon gas were purchased from Praxair. Deionized water (DI water with 18.2 MΩ·cm, <5 ppb TOC) was obtained from a Millipore water system. Isotope labeled $^{13}CH_3I$ (99%) was purchased from Cambridge Isotope Laboratories, Inc. Fumasep and Selemion AMV anion exchange membrane was ordered from Fuel Cell Store and AGC Engineering.

Electrode preparation

The electrochemical polish parameter in the previous report[50] was used here. Specifically, the as-received Cu foil was first cut to the desired size, then sonicated in an ethanol bath and DI water bath sequentially in order to remove the organic contamination on the Cu surface. Then the Cu foil was dipped into the 85% o-phosphoric acid and electrochemically polished with a carbon rod as the counter electrode. The electrochemical polish process would last for 10 min under the applied potential of 2.1V vs carbon rod. After the electrochemical polish, Cu foil was rinsed with DI water to remove acid on the surface and then blow-dried with Ar flow. The prepared EC-Cu is then immediately used for the characterization of electrochemical tests.

For Cu and Ag NP synthesis, previously reported recipes were followed[44-46]. NPs were spin-coated on the glassy carbon planchet, and this process was optimized to load NPs close to a monolayer. To form a tandem NP system, Cu and Ag NP solutions were mixed and spin-coated on the support by using a spin coater (Laurell WS-400A-6NPP/LITE). For instance, to make Cu50Ag50 where 50% of the total number of NPs was Cu NPs, the concentration of each Cu and Ag NP solution was taken into account when a mixed solution was prepared. The active area of the electrode exposed to the electrolyte was 1.13 cm^2.

Characterization

The images of Cu surface morphology were acquired by using an FEI Quanta 3D FEG/FIB SEM with the operation condition of 5 kV and 3.4 nA. X-ray photoelectron spectroscopy (XPS) (Thermo Scientific K-Alpha) characterization was conducted using an Al Kα source. In order to measure the post-electrolysis sample, EC-Cu foil was sampled after CH_3I and CO co-reduction under -0.8 V vs RHE for 6 h. The foil was then rinsed with DI water to remove as much electrolyte residue as possible and blow-dried with Ar flow. Post electrolysis SEM

images of the Cu-Ag nanoparticles were directly collected on the glassy carbon substrate after the CO_2RR is finished. For TEM based characterizations, particles were redispersed in ethanol by ultrasonication, then deposit on the TEM grids. Atomic-scale high-angle annular dark-field detector scanning transmission electron microscopy (HAADF-STEM) images and elemental electron energy loss spectroscopy (EELS) maps were acquired on a fifth-order aberration-corrected STEM (Cornell Nion UltraSTEM) operated at 100 keV with a beam convergence semi-angle of 30 mrad. Sub-Ångström spatial resolution is achievable under such operating conditions. EELS spectral images were acquired with a 0.25 eV/channel energy dispersion (energy resolution, 1.0 eV) in a Gatan spectrometer with a size of 100 pixels and an acquisition time of 10 ms/pixel. EELS spectrum images were processed using principal component analysis (PCA, 3 components) and the linear combination of power law (LCPL) to subtract the background, in ImageJ software. In addition, the energy dispersive X-ray (EDX) mapping was acquired in STEM mode using the Titan Themis microscope at National Center for Electron Microscopy (NCEM) at LBNL. STEM-EDX maps were acquired for 30-40 min with drift correction using the Velox software and an estimated spatial resolution of 1-2 nm at 300 keV and about 0.6 nA beam current using a quadruple Bruker EDX detector with a large solid angle of 0.7 steradian. High-resolution bright-field TEM (HR-TEM) images were also acquired on Themis at 300 keV.

Electrochemical tests

Electrochemical tests were conducted in conventional H-cells. For all the CH_3I and CO related experiments, the cathode and anode of the H-cell were separated by an anion exchange membrane. The volume of electrolyte in both chambers was 50 ml. Before electrolysis, the electrolyte was firstly bubbled with carrier gases for at least 20 min to remove dissolved oxygen. 0.1 M $KHCO_3$ was used as the default electrolyte unless specific conditions are stated. The gas flow rate during electrolysis was controlled at 10 ml/min by a mass flow controller at room temperature. Ag/AgCl (3 M KCl) was used as the reference electrode. For NP based CO_2RR experiments, the volume of the electrolyte in both chambers was 17 ml while the gas flow rate was 20 ml/min. Besides that, other operating conditions and procedures were identical.

In double-layer capacitance measurement, gas flow and stir bar were stopped after the system was fully deoxygenated. Meanwhile, the gas outlet was also sealed. The potential range of cyclic voltammetry (CV) scans was set from -0.1 V to 0.25 V vs RHE. Through linear regression, the slope of the charging and discharging currents with respect to the scan rates was obtained, which corresponds to the surface's double-layer capacitance.

The polarization response curves were also collected with CV technique. After the CV curve was stable (usually after 5 loops), the cathodic scan sections between 0.1 V and -0.9 V vs RHE were then collected and plotted for comparison. 10 µl CH_3I was added to the electrolyte for the investigation of the characteristic reduction peak and operation window of CH_3IRR.

Catalytic performances were tested with 85% iR compensated chronoamperometry (CA). The remaining 15% iR drop was manually compensated during the data analysis. The deviation of actual potential from expected potential is normally smaller than 25 mV, which is not supposed to influence any of the comparison or conclusions in this study relative to the 200 mV or 150 mV intervals applied in the electrochemical tests. For both ^{12}CO and $^{13}CH_3I$ co-reduction and $^{12}CO_2$ and $^{13}CH_3I$ co-reduction experiments, while the gas flow was kept constant during the 6 h electrolysis, two doses of 50 µl of CH_3I were added to the cathodic chamber at 0 h and 3 h, respectively. Because of the hazards associated with handling CH_3I (i.e., volatile and highly toxic), all CH_3I relevant operations need to be performed in a fume hood accordingly. During each 3 h electrolysis period, the current gradually decreased due to the consumption of CH_3I reduction as well as CH_3I evaporation with gas flow. All gases eluting from the outlet were cumulated in a gas bag during the electrolysis in order to obtain an averaged result. Liquid products were sampled after 6 h electrolysis. For CO reduction reaction without CH_3I, gas can directly be sampled from headspace with a syringe, and a gas bag is no longer necessary. In the KI involved control experiment, 267 mg of fresh KI was dissolved in the catholyte to match up with the fed-in I in the co-reduction experiments. Other than the addition of KI, the setup and operations of the control experiment are all the same as routine CO reduction reactions.

Product analysis

After electrolysis, gas products, including CO, CH_4, C_2H_4, C_2H_6, and H_2 were detected and quantified using gas chromatography (Agilent 7890B GC system). An additional 10 min baking at 200ºC was added into the GC program to remove the CH_3I vapor trapped in the column. For NP based CO_2 electrolysis, gas products were measured by gas chromatography (SRI MG3) equipped with a thermal conductivity detector and a flame ionization detector. Liquid products were analyzed by ^1H nuclear magnetic resonance spectroscopy (Bruker AV600 with a 5 mm Z-gradient triple resonance ^1H/BB Prodigy cryo-probe) with water suppression by excitation sculpting. 900 µl aliquot and 100 µl DMSO-D_2O solution were mixed for locking purposes, in which DMSO was used as the internal standard for quantification.

Data availability

All data is available from the authors upon reasonable request.

AUTHOR INFORMATION

Corresponding Author:

*Peidong Yang; Email: p_yang@berkeley.edu

Acknowledgments

This work was supported by Director, Office of Science, Office of Basic Energy Sciences, Chemical Sciences, Geosciences, & Biosciences Division, of the US Department of Energy under Contract DE-AC02-05CH11231, FWP CH030201 (Catalysis Research Program). STEM-EDX and XPS were conducted using facilities at the Molecular Foundry. Work at the Molecular Foundry was supported by the Office of Science, Office of Basic Energy Sciences, of the U.S. Department of Energy under Contract No. DE-AC02-05CH11231. The STEM-EELS work made use of TEM facilities (Nion UltraSTEM) at the Cornell Center for Materials Research (CCMR), which are supported through the National Science Foundation Materials Research Science and Engineering Center (NSF MRSEC) program (DMR-1719875). We thank the TEM technical support of Drs. Rohan Dhall, Karen Bustillo at NCEM and Mick Thomas at Cornell. We thank Dr. Hasan Celik and UC Berkeley's NMR facility in the College of Chemistry (CoC-NMR) for spectroscopic assistance. Instruments in the CoC-NMR are supported in part by NIH S10OD024998. C.C. and J.J. gratefully acknowledge support from Suzhou Industrial Park Scholarship. S.Y. acknowledges support from Samsung Scholarship. Y.Y. acknowledges support from Miller Research Fellowship. P.-C.C. acknowledges support from Kavli ENSI Heising-Simons Fellowship.

Author Contributions

C.C., S.Y., and P.Y. conceived the research and designed the experiments. C.C. conducted the isotope labeling experiments, and S.Y. conducted nanoparticle synthesis and CO_2 electrolysis with assistance from S.L., I.R., S.C., and Y.S. Electron microscopy characterization and structural analysis were conducted by Y.Y. and P.C. All authors contributed to the discussion of the experimental results and the preparation of the manuscript.

Competing Interests

The authors declare no competing interests.

Figure captions

Fig. 1. Asymmetric C-C coupling pathways in biological carbon fixation and inorganic CO_2 electroreduction. a, Schematic illustration of $*CH_3$-*CO asymmetric coupling in the Wood-Ljungdahl pathway as a natural CO_2 bio-fixation process. In the Wood-Ljungdahl pathway, corrinoid iron-sulfur protein (CFeSP) delivers a methyl group derived from CO_2 to carbon monoxide dehydrogenase (CODH)/Acetyl-CoA Synthase (ACS) where CO_2 is converted to *CO and further combined with the $*CH_3$ and coenzyme-A (CoA), leading to the synthesis of acetyl-CoA (CH_3COS-CoA) and finally the generation of acetic acid. **b**, Schematic illustration of symmetric and underexplored asymmetric coupling process in inorganic CO_2 electroreduction. **c**, In this study, isotope labeled intermediates are externally fed to verify the existence of the asymmetric coupling process on a Cu surface. Afterward, a Cu-Ag nanoparticle assembly is used to generate asymmetric coupling intermediates internally in CO_2 electroreduction, demonstrating the feasibility of the asymmetric C-C coupling mechanism in CO_2 reduction with inorganic catalysts.

Fig. 2. Electrocatalytic dehalogenation of CH_3I under negative bias. a, The polarization response curve on the EC-Cu and glassy carbon electrodes with and without CH_3I in 0.1 M $KHCO_3$. **b**, The pH independence of characteristic CH_3I reduction peak position on EC-Cu against the SHE scale. **c**, Potential dependent Faraday efficiency (FE) of different CH_3IRR products and their corresponding current densities during CH_3I electroreduction on EC-Cu.

Fig. 3. Potential dependent CO reduction experiments and $^{13}CH_3I$ and ^{12}CO co-reduction experiments on EC-Cu. a,**b**, Potential dependent product FEs and corresponding current density (**a**) and multicarbon oxygenate production amounts and distribution after 6 hours electrolysis (**b**) of CO electroreduction on EC-Cu. **c**,**d**, Potential dependent product FEs and corresponding current density (**c**) and multicarbon oxygenate production amounts and distribution after 6 hours electrolysis (**d**) of ^{12}CO and $^{13}CH_3I$ co-reduction (**d**) on EC-Cu. Asymmetric products are quantified by isotope experiments. Error bars represent standard deviations based on three separate experiments, with the center being the mean. The loss of FE under -0.2 V and -0.4 V vs RHE in the CORR is due to the low current densities on EC-Cu. **e**, NMR spectra of liquid products from CH_3I and CO co-reduction experiments. Identified peaks are

labeled with corresponding products. The blue color is used to highlight the products/protons that are related to C-12 while the red color is used for C-13. Unidentified minor peaks are labeled with diamond marks, which may come from trace impurities in the CH_3I reagent and CH_3I-induced leaching of the rubber sealing components. It is clear that no coupling reaction happens at the open circuit potential, which shows a flat baseline. $^{13}CH_3OH$ mainly comes from the hydrolysis of $^{13}CH_3I$, which is not the target product in this study.

Fig. 4. Cu-Ag tandem CO_2 electrolysis optimization via asymmetric coupling. a,**b**, TEM images of 7nm Cu NPs (**a**) and 7nm Ag NPs (**b**). **c**, SEM image of as-prepared Cu-Ag NP assembly on glassy carbon as the working electrode. **d**, Potential dependent production rates of CO and CH_4 as two intermediate indicators in CO_2 reduction on Cu-Ag NP assembly electrodes with varied Cu-Ag ratios. **e**, Potential dependent multicarbon oxygenate production rates in CO_2 reduction on Cu-Ag NP assembly electrodes with varied Cu-Ag ratios. The co-existence of CH_4 and CO is a dimensionless indicator defined as the minimum value between CO and CH_4 production rates, which indicates the limiting factor for asymmetric coupling. All potentials here are described under the RHE scale.

References

1. Jordaan, S. M., Wang, C. Electrocatalytic conversion of carbon dioxide for the Paris goals. *Nat. Catal.* **4**, 915-920 (2021).
2. Ross, M. B. et al. Designing materials for electrochemical carbon dioxide recycling. *Nat. Catal.* **2**, 648-658 (2019).
3. Habisreutinger, S. N., Schmidt-Mende, L., Stolarczyk, J. K. Photocatalytic reduction of CO_2 on TiO_2 and other semiconductors. *Angew. Chem. Int. Ed.* **52**, 7372-408 (2013).
4. Jasniewski, A. J., Lee, C. C., Ribbe, M. W., Hu, Y. Reactivity, mechanism, and assembly of the alternative nitrogenases. *Chem. Rev.* **120**, 5107-5157 (2020).
5. Marques Mota, F., Kim, D. H. From CO_2 methanation to ambitious long-chain hydrocarbons: alternative fuels paving the path to sustainability. *Chem. Soc. Rev.* **48**, 205-259 (2019).
6. Can, M., Armstrong, F. A., Ragsdale, S. W. Structure, function, and mechanism of the nickel metalloenzymes, CO dehydrogenase, and acetyl-CoA synthase. *Chem. Rev.* **114**, 4149-4174 (2014).
7. Ragsdale, S. W., Pierce, E. Acetogenesis and the Wood-Ljungdahl pathway of CO_2 fixation. *Biochim. Biophys. Acta* **1784**, 1873-1898 (2008).
8. Nitopi, S. et al. Progress and perspectives of electrochemical CO_2 reduction on copper in aqueous electrolyte. *Chem. Rev.* **119**, 7610-7672 (2019).
9. Hori, Y., Murata, A., Takahashi, R. Formation of hydrocarbons in the electrochemical reduction of carbon dioxide at a copper electrode in aqueous solution. *J. Chem. Soc., Faraday Trans. 1* **85**, 2309-2326 (1989).
10. Montoya, J. H., Shi, C., Chan, K., Norskov, J. K. Theoretical insights into a CO dimerization mechanism in CO_2 electroreduction. *J. Phys. Chem. Lett.* **6**, 2032-2037 (2015).
11. Wang, L. et al. Electrochemical carbon monoxide reduction on polycrystalline copper: effects of potential, pressure, and pH on selectivity toward multicarbon and oxygenated products. *ACS Catal.* **8**, 7445-7454 (2018).
12. Hanselman, S., Koper, M. T. M., Calle-Vallejo, F. Computational comparison of late transition metal (100) surfaces for the electrocatalytic reduction of CO to C_2 species. *ACS Energy Lett.* **3**, 1062-1067 (2018).
13. Perez-Gallent, E., Figueiredo, M. C., Calle-Vallejo, F., Koper, M. T. Spectroscopic observation of a hydrogenated CO dimer intermediate during CO reduction on Cu(100) electrodes. *Angew. Chem. Int. Ed.* **56**, 3621-3624 (2017).
14. Kim, Y. et al. Time-resolved observation of C–C coupling intermediates on Cu electrodes for selective electrochemical CO_2 reduction. *Energy Environ. Sci.* **13**, 4301-4311 (2020).
15. Xiao, H., Cheng, T., Goddard, W. A., Sundararaman, R. Mechanistic explanation of the pH dependence and onset potentials for hydrocarbon products from electrochemical reduction of CO on Cu (111). *J. Am. Chem. Soc.* **138**, 483-486 (2016).
16. Xiao, H., Cheng, T., Goddard, W. A. Atomistic mechanisms underlying selectivities in C_1 and C_2 products from electrochemical reduction of CO on Cu(111). *J. Am. Chem. Soc.* **139**, 130-136 (2017).
17. Zhao, Q., Martirez, J. M. P., Carter, E. A. Revisiting understanding of electrochemical CO_2 reduction on Cu(111): competing proton-coupled electron transfer reaction mechanisms revealed by embedded correlated wavefunction theory. *J. Am. Chem. Soc.* **143**, 6152-6164 (2021).
18. Ma, W. et al. Electrocatalytic reduction of CO_2 to ethylene and ethanol through hydrogen-assisted C–C coupling over fluorine-modified copper. *Nat. Catal.* **3**, 478-487 (2020).
19. Choi, C. et al. Highly active and stable stepped Cu surface for enhanced electrochemical CO_2 reduction to C_2H_4. *Nat. Catal.* **3**, 804-812 (2020).
20. Garza, A. J., Bell, A. T., Head-Gordon, M. Mechanism of CO_2 reduction at copper surfaces: pathways to C_2 products. *ACS Catal.* **8**, 1490-1499 (2018).
21. Schouten, K. J., Qin, Z., Perez Gallent, E., Koper, M. T. Two pathways for the formation of ethylene in CO reduction on single-crystal copper electrodes. *J. Am. Chem. Soc.* **134**, 9864-9867 (2012).

22. Cheng, T., Xiao, H., Goddard, W. A. Full atomistic reaction mechanism with kinetics for CO reduction on Cu(100) from ab initio molecular dynamics free-energy calculations at 298 K. *Proc. Natl. Acad. Sci. U. S. A.* **114**, 1795-1800 (2017).
23. Dinh, C.-T. et al. CO_2 electroreduction to ethylene via hydroxide-mediated copper catalysis at an abrupt interface. *Science* **360**, 783-787 (2018).
24. Luc, W. et al. Two-dimensional copper nanosheets for electrochemical reduction of carbon monoxide to acetate. *Nat. Catal.* **2**, 423-430 (2019).
25. Kim, C. et al. Tailored catalyst microenvironments for CO_2 electroreduction to multicarbon products on copper using bilayer ionomer coatings. *Nat. Energy* **6**, 1026-1034 (2021).
26. Vasileff, A. et al. Electrochemical reduction of CO_2 to ethane through stabilization of an ethoxy intermediate. *Angew. Chem. Int. Ed.* **132**, 19817-19821 (2020).
27. Ren, D., Ang, B. S.-H., Yeo, B. S. Tuning the selectivity of carbon dioxide electroreduction toward ethanol on oxide-derived Cu_xZn catalysts. *ACS Catal.* **6**, 8239-8247 (2016).
28. Iyengar, P., Kolb, M. J., Pankhurst, J. R., Calle-Vallejo, F., Buonsanti, R. Elucidating the facet-dependent selectivity for CO_2 electroreduction to ethanol of Cu–Ag tandem catalysts. *ACS Catal.* **11**, 4456-4463 (2021).
29. Ting, L. R. L., Piqué, O., Lim, S. Y., Tanhaei, M., Calle-Vallejo, F., Yeo, B. S. Enhancing CO_2 electroreduction to ethanol on copper–silver composites by opening an alternative catalytic pathway. *ACS Catal.* **10**, 4059-4069 (2020).
30. Raaijman, S. J., Schellekens, M. P., Corbett, P. J., Koper, M. T. M. High-pressure CO electroreduction at silver produces ethanol and propanol. *Angew. Chem. Int. Ed.* **60**, 21732-21736 (2021).
31. Kas, R., Ayemoba, O., Firet, N. J., Middelkoop, J., Smith, W. A., Cuesta, A. In‐situ infrared spectroscopy applied to the study of the electrocatalytic reduction of CO_2: theory, practice and challenges. *ChemPhysChem* **20**, 2904-2925 (2019).
32. Sebastián-Pascual, P., Escudero-Escribano, M. Surface characterization of copper electrocatalysts by lead underpotential deposition. *J. Electroanal. Chem.* **896**, 115446 (2021).
33. Chen, Y. Recent advances in methylation: a guide for selecting methylation reagents. *Chem. Eur. J.* **25**, 3405-3439 (2019).
34. Zhang, W. et al. Electrochemically driven cross-electrophile coupling of alkyl halides. *Nature* **604**, 292-297 (2022).
35. Fedurco, M., Sartoretti, C. J., Augustynski, J. Reductive cleavage of the carbon−halogen bond in simple methyl and methylene halides. reactions of the methyl radical and carbene at the polarized electrode/aqueous solution interface. *Langmuir* **17**, 2380-2387 (2001).
36. Lin, J. L., Bent, B. E. Two mechanisms for formation of methyl radicals during the thermal decomposition of methyl iodide on a copper surface. *J. Phys. Chem.* **97**, 9713-9718 (1993).
37. Lei, C., Liang, F., Li, J., Chen, W., Huang, B. Electrochemical reductive dechlorination of chlorinated volatile organic compounds (Cl-VOCs): Effects of molecular structure on the dehalogenation reactivity and mechanisms. *Chem. Eng. J.* **358**, 1054-1064 (2019).
38. Gunathunge, C. M., Ovalle, V. J., Li, Y., Janik, M. J., Waegele, M. M. Existence of an electrochemically inert CO population on Cu electrodes in alkaline pH. *ACS Catal.* **8**, 7507-7516 (2018).
39. Li, J., Li, X., Gunathunge, C. M., Waegele, M. M. Hydrogen bonding steers the product selectivity of electrocatalytic CO reduction. *Proc. Natl. Acad. Sci. U.S.A.* **116**, 9220-9229 (2019).
40. Chang, X., Malkani, A., Yang, X., Xu, B. Mechanistic insights into electroreductive C-C Coupling between CO and acetaldehyde into multicarbon products. *J. Am. Chem. Soc.* **142**, 2975-2983 (2020).
41. Van Santen, R., Markvoort, A., Filot, I., Ghouri, M., Hensen, E. Mechanism and microkinetics of the Fischer–Tropsch reaction. *Phys. Chem. Chem. Phys.* **15**, 17038-17063 (2013).
42. Zhao, Y., Cui, C., Han, J., Wang, H., Zhu, X., Ge, Q. Direct C–C coupling of CO_2 and the methyl group from CH_4 activation through facile insertion of CO_2 into Zn–CH_3 σ-bond. *J. Am. Chem. Soc.* **138**, 10191-10198 (2016).
43. Zhao, Y., Wang, H., Han, J., Zhu, X., Ge, Q. Active site ensembles enabled C–C coupling of CO_2 and CH_4 for acetone production. *J. Phys. Chem. C* **122**, 9570-9577 (2018).
44. Kim, D. et al. Selective CO_2 electrocatalysis at the pseudocapacitive nanoparticle/ordered-ligand interlayer. *Nat. Energy* **5**, 1032-1042 (2020).
45. Hung, L. I., Tsung, C. K., Huang, W., Yang, P. Room‐temperature formation of hollow Cu_2O nanoparticles. *Adv. Mater.* **22**, 1910-1914 (2010).
46. Kim, D., Kley, C. S., Li, Y., Yang, P. Copper nanoparticle ensembles for selective electroreduction of CO_2 to C_2–C_3 products. *Proc. Natl. Acad. Sci. U.S.A.* **114**, 10560-10565 (2017).
47. Manthiram, K., Beberwyck, B. J., Alivisatos, A. P. Enhanced electrochemical methanation of carbon dioxide with a dispersible nanoscale copper catalyst. *J. Am. Chem. Soc.* **136**, 13319-13325 (2014).
48. Huang, J., Mensi, M., Oveisi, E., Mantella, V., Buonsanti, R. Structural sensitivities in bimetallic catalysts for electrochemical CO_2 reduction revealed by Ag-Cu nanodimers. *J. Am. Chem. Soc.* **141**, 2490-2499 (2019).
49. Gu, J., Hsu, C.-S., Bai, L., Chen, H. M., Hu, X. Atomically dispersed Fe^{3+} sites catalyze efficient CO_2 electroreduction to CO. *Science* **364**, 1091-1094 (2019).
50. Wang, L. et al. Selective reduction of CO to acetaldehyde with CuAg electrocatalysts. *Proc. Natl. Acad. Sci. U. S. A.* **117**, 12572-12575 (2020).

a

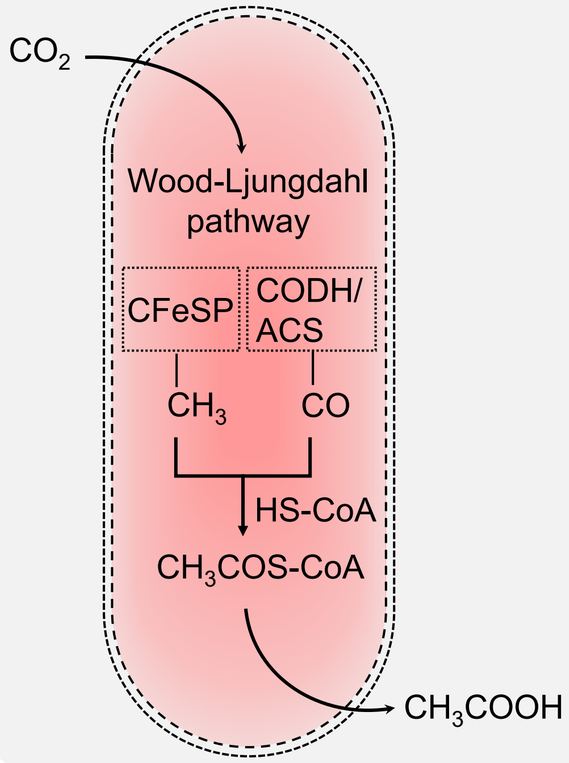
CO_2
Wood-Ljungdahl pathway
CFeSP
CODH/ ACS
CH_3
CO
HS-CoA
CH_3COS-CoA
CH_3COOH

b

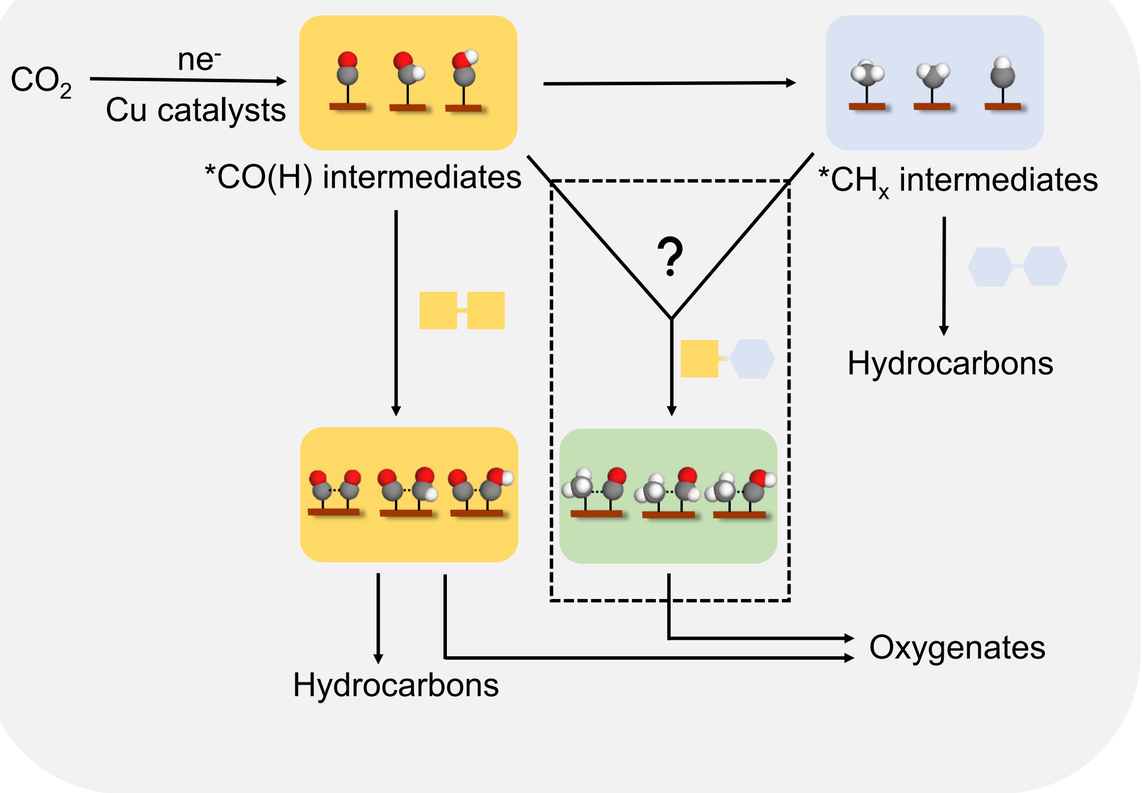
CO_2
ne-
Cu catalysts
*CO(H) intermediates
*CH_x intermediates
?
Hydrocarbons
Hydrocarbons
Oxygenates

C

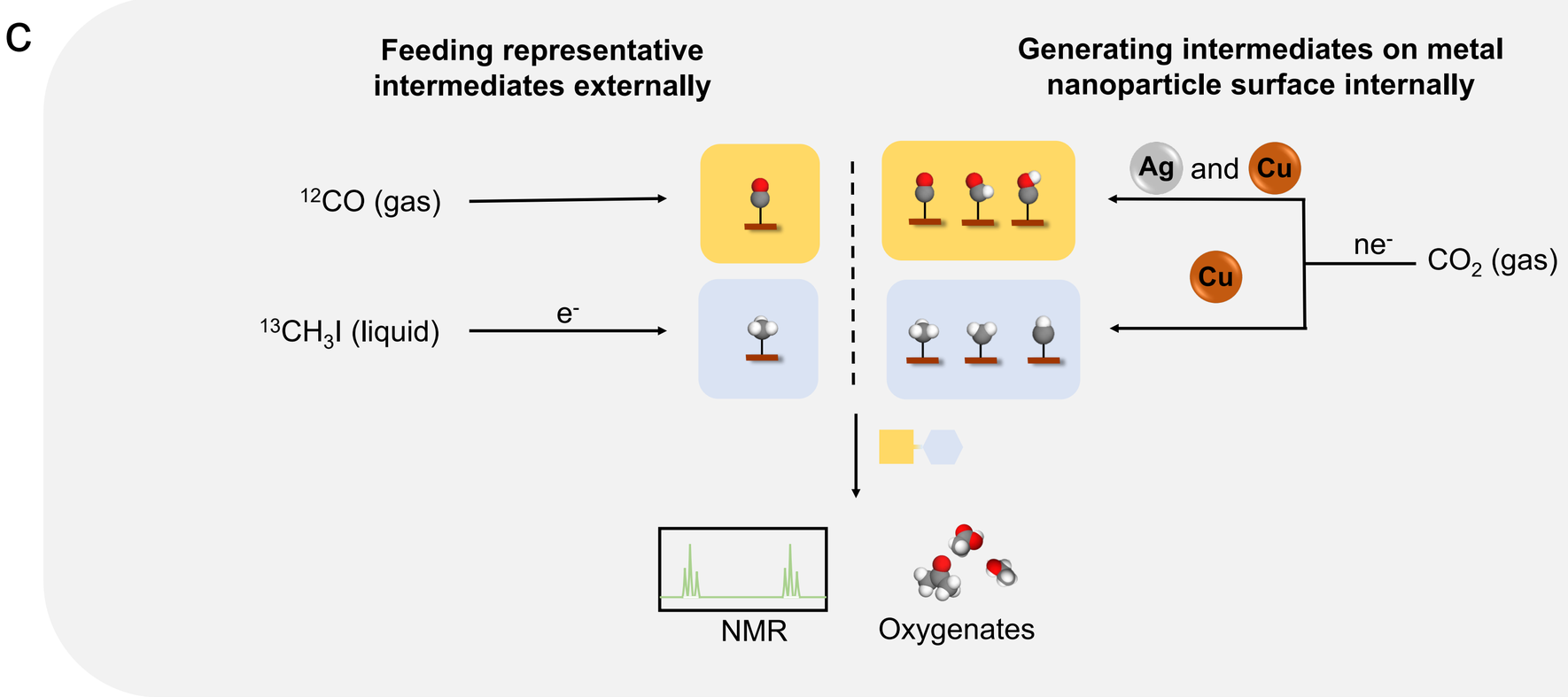
Feeding representative intermediates externally
Generating intermediates on metal nanoparticle surface internally
^{12}CO (gas)
$^{13}CH_3I$ (liquid)
e-
Ag and Cu
Cu
ne-
CO_2 (gas)
NMR
Oxygenates

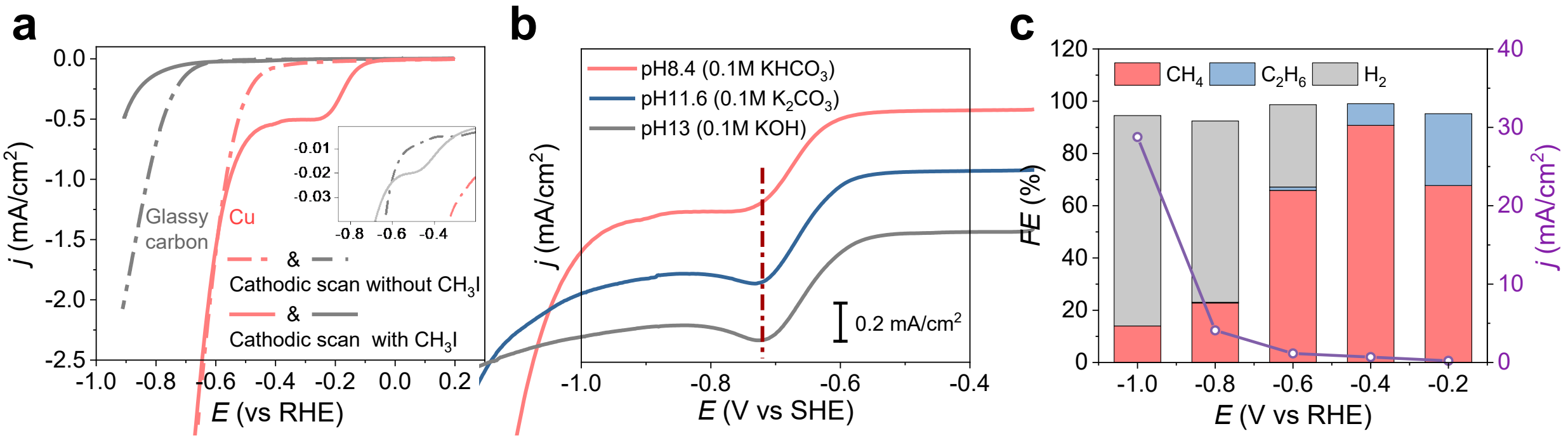
a
b
c
j (mA/cm2)
E (vs RHE)
Glassy carbon
Cu
Cathodic scan without CH3I
&
Cathodic scan with CH3I
pH8.4 (0.1M KHCO3)
pH11.6 (0.1M K2CO3)
pH13 (0.1M KOH)
0.2 mA/cm2
E (V vs SHE)
FE (%)
CH4
C2H6
H2
j (mA/cm2)
E (V vs RHE)

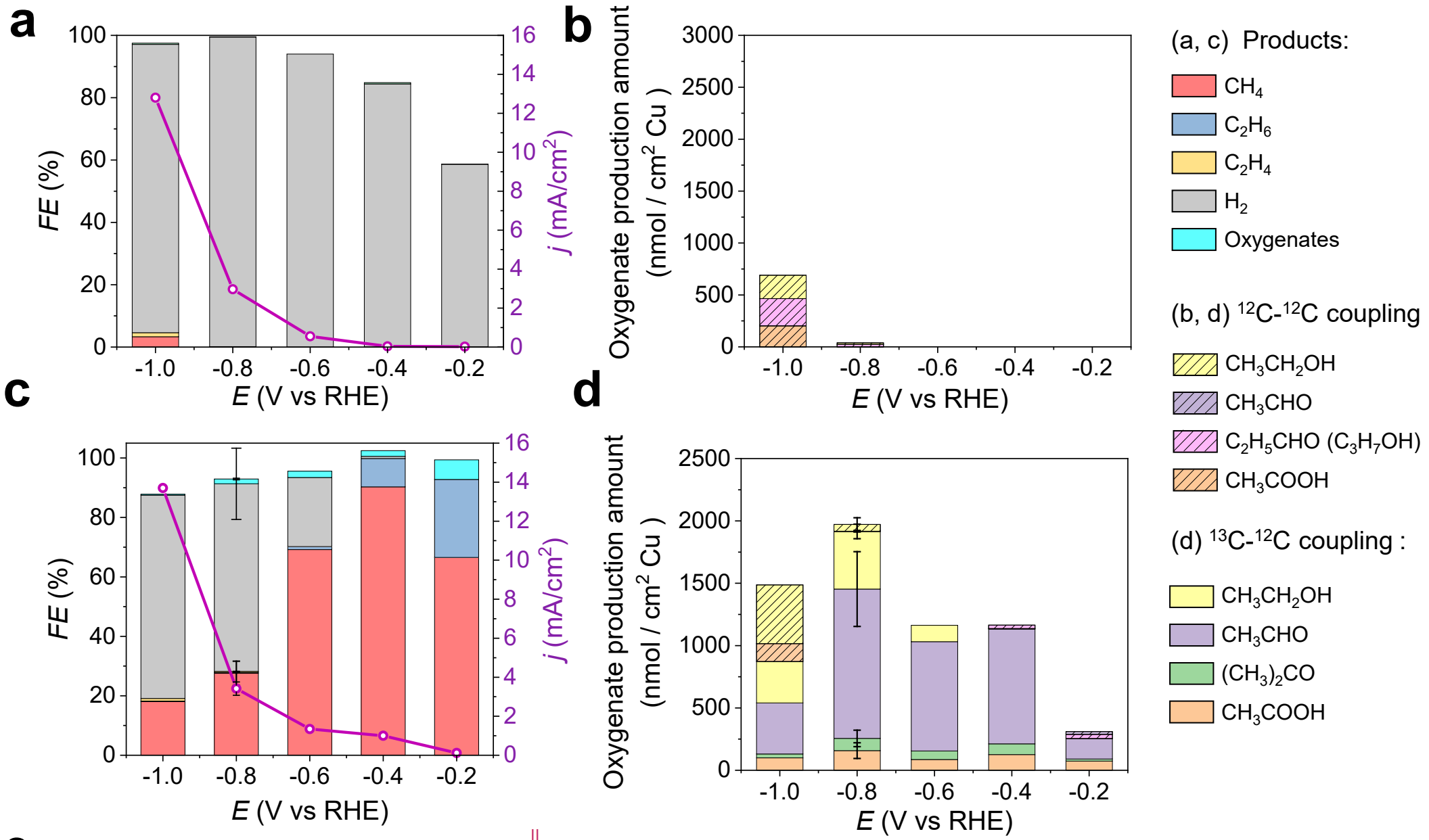
a
FE (%)
j (mA/cm²)
E (V vs RHE)
b
Oxygenate production amount (nmol / cm² Cu)
E (V vs RHE)
(a, c) Products:
CH4
C2H6
C2H4
H2
Oxygenates
(b, d) 12C-12C coupling :
CH3CH2OH
CH3CHO
C2H5CHO (C3H7OH)
CH3COOH
c
FE (%)
j (mA/cm²)
E (V vs RHE)
d
Oxygenate production amount (nmol / cm² Cu)
E (V vs RHE)
(d) 13C-12C coupling :
CH3CH2OH
CH3CHO
(CH3)2CO
CH3COOH
e
DMSO (internal standard)
13CH3I and 12CO co-reduction

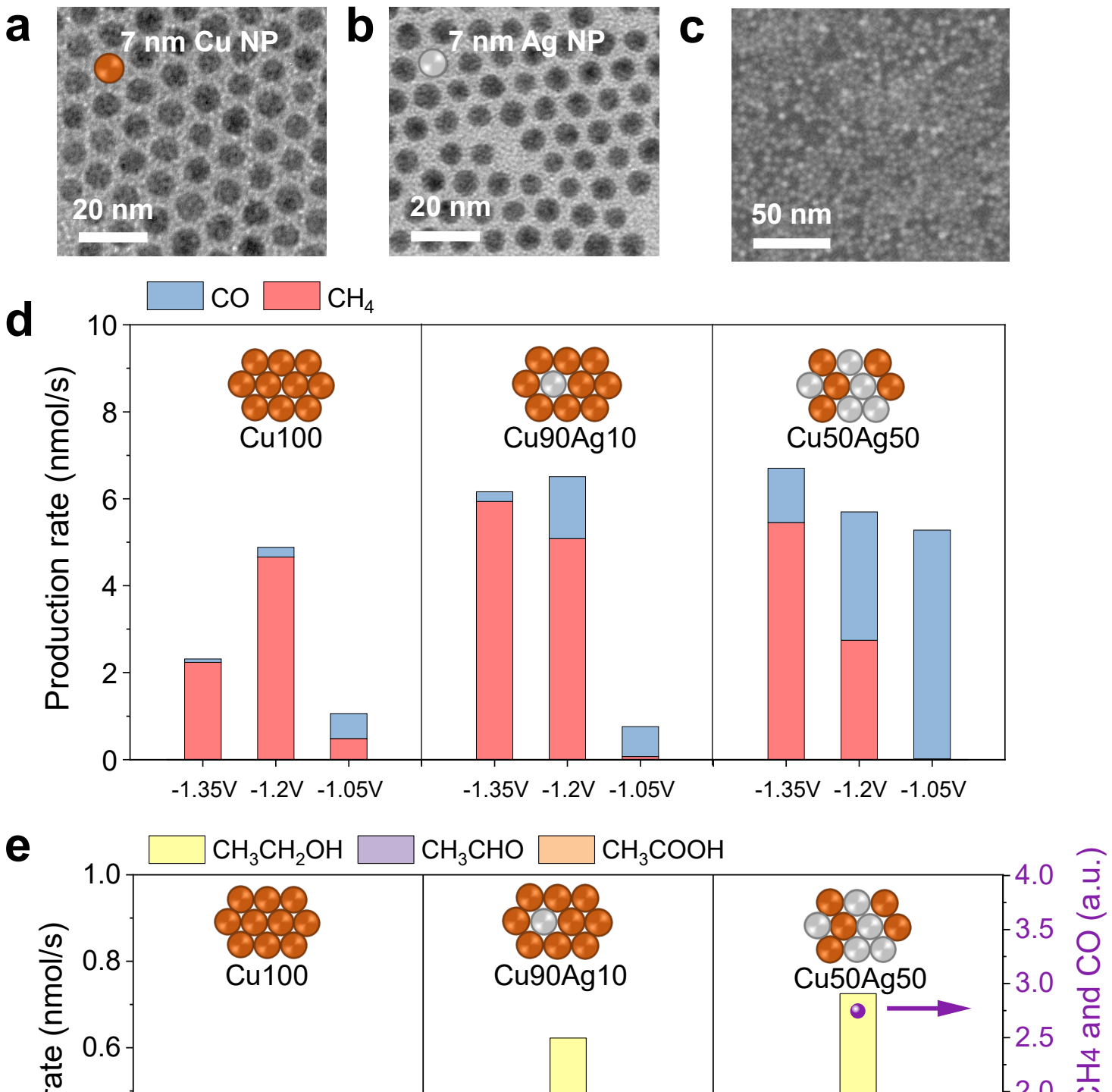
a
7 nm Cu NP
20 nm
b
7 nm Ag NP
20 nm
c
50 nm
d
CO
CH4
Production rate (nmol/s)
Cu100
Cu90Ag10
Cu50Ag50
-1.35V
-1.2V
-1.05V
e
CH3CH2OH
CH3CHO
CH3COOH
Cu100
Cu90Ag10
Cu50Ag50
CH4 and CO (a.u.)